

Powder diffraction from a continuous microjet of submicrometer protein crystals

D. A. Shapiro,^{a,b*} H. N. Chapman,^{c,‡} D. DePonte,^d R. B. Doak,^d P. Fromme,^e G. Hembree,^d M. Hunter,^e S. Marchesini,^{a,b} K. Schmidt,^d J. Spence,^d D. Starodub^d and U. Weierstall^d

^aAdvanced Light Source, Lawrence Berkeley National Laboratory, Berkeley, CA 94720, USA,

^bCenter For Biophotonics Science and Technology, University of California at Davis, 2700 Stockton Blvd, Suite 1400, Sacramento, CA 95817, USA, ^cLawrence Livermore National Laboratory, 7000 East Avenue, Livermore, CA 94550, USA, ^dDepartment of Physics, Arizona State University, Tempe, AZ 85287, USA, and ^eDepartment of Chemistry and Biochemistry, Arizona State University, Tempe, AZ 85287, USA. E-mail: dashapiro@lbl.gov

Atomic-resolution structures from small proteins have recently been determined from high-quality powder diffraction patterns using a combination of stereochemical restraints and Rietveld refinement [Von Dreele (2007), *J. Appl. Cryst.* **40**, 133–143; Margiolaki *et al.* (2007), *J. Am. Chem. Soc.* **129**, 11865–11871]. While powder diffraction data have been obtained from batch samples of small crystal-suspensions, which are exposed to X-rays for long periods of time and undergo significant radiation damage, the proof-of-concept that protein powder diffraction data from nanocrystals of a membrane protein can be obtained using a continuous microjet is shown. This flow-focusing aerojet has been developed to deliver a solution of hydrated protein nanocrystals to an X-ray beam for diffraction analysis. This method requires neither the crushing of larger polycrystalline samples nor any techniques to avoid radiation damage such as cryocooling. Apparatus to record protein powder diffraction in this manner has been commissioned, and in this paper the first powder diffraction patterns from a membrane protein, photosystem I, with crystallite sizes of less than 500 nm are presented. These preliminary patterns show the lowest-order reflections, which agree quantitatively with theoretical calculations of the powder profile. The results also serve to test our aerojet injector system, with future application to femtosecond diffraction in free-electron X-ray laser schemes, and for serial crystallography using a single-file beam of aligned hydrated molecules.

1. Introduction

The major bottleneck in protein structure determination by X-ray diffraction from single crystals is the production of high-quality crystals that are large enough for diffraction analysis. Protein crystallography beamlines that utilize third-generation synchrotron sources typically require crystals that are at least 20 μm in size for the collection of atomic-resolution data. Even microdiffraction probes are limited to crystals several tens of micrometers in size, since the high X-ray exposure of small single crystals leads to the severe problem of radiation damage. Most membrane protein crystals suffer X-ray damage during data collection even at cryogenic temperatures. Small

single crystals of membrane proteins fail to show high-resolution X-ray diffraction after seconds of exposure so data have to be collected using hundreds of partial data sets from many crystals. That method has been used to determine the first high-resolution structure of G-protein coupled receptor (Rasmussen *et al.*, 2007), a class of membrane proteins that represent more than 50% of all current drug targets. Alternatively, data collection has to be performed using large single crystals that can be shifted several times to limit the X-ray exposure at each region of the crystal.

The size of the crystals required for data collection increases with the size of the unit cell. As an example, crystals larger than 500 μm were essential for the structure determination of photosystem I at 2.5 Å resolution (Jordan *et al.*, 2001). Photosystem I is a membrane protein with a molecular

[‡] Current address: Centre for Free-Electron Laser Science, Universität Hamburg and DESY, Notkestrasse 85, 22607 Hamburg, Germany.

weight of 1.056 MDa and represents one example of a class of proteins that are difficult to crystallize. The production of large well ordered single crystals of proteins that are difficult to crystallize can take years and may involve very time-consuming investigations such as the determination of phase diagrams or seeding techniques. At the same time, optical microscopy evidence suggests that many crystallization solutions may contain large numbers of small crystals of size $\sim 1 \mu\text{m}$ or smaller (Von Driel, 2007), and the mother liquor in crystal growth wells contains a high concentration of these nuclei. Experiment and theory indicate that such small crystals do not contain enough molecules for statistically significant scattering before destruction of high-resolution detail by radiation damage. These considerations have led to a revival of interest in powder protein crystallography (Margiolaki & Wright, 2008).

In this paper we report preliminary results from a serial protein crystallography project that aims to provide a proof of concept that X-ray diffraction can be detected from a stream of droplets that contains nanocrystals. As the model protein we did not choose lysozyme, but photosystem I, which is the largest and most complex membrane protein that has been crystallized to date. The central component of this method is a single-file droplet beam, containing nanocrystals, which originates from a gas dynamic virtual nozzle (aerojet) (DePonte *et al.*, 2008; Weierstall *et al.*, 2008) droplet source and traverses a quasi-continuous X-ray beam. The jet may be filled directly with mother liquor from crystal growth cells, allowing us both to test the jet and evaluate the prospects for using it for powder protein diffraction. The current experiment is limited in resolution only by the long wavelength of the X-rays used, but the method shows potential for high-throughput screening of crystallization drops for microcrystals and the avoidance of radiation damage during collection of powder diffraction data.

Since the droplets are moving with a velocity of the order of 10 m s^{-1} and the X-ray beam is only a few tens of micrometers wide, each protein nanocrystal is exposed to X-rays for only $2 \mu\text{s}$ and thus is not damaged by the ionizing radiation. Using tabulated data for elemental photoabsorption cross sections (Henke *et al.*, 1993), we obtain a mass absorption coefficient $\mu = 6.1 \times 10^4 \text{ cm}^2 \text{ g}^{-1}$ at an X-ray energy $E = 530 \text{ eV}$ for a generic protein stoichiometry $\text{H}_{50}\text{C}_{30}\text{N}_9\text{O}_{10}\text{S}_1$. The energy per unit mass (dose) deposited into a protein nanocrystal during its passage through the X-ray beam can be estimated as $D = \mu EI_0 t = 1.3 \times 10^3 \text{ Gy}$, where I_0 is the incident X-ray flux (number of photons incident per unit area per unit time). This dose is more than four orders of magnitude lower than the Henderson limit, therefore radiation damage is not a concern in our experiments. Large total exposure times are therefore available without damaging the sample because the detector integrates the diffracted intensity as the crystallites are continuously refreshed by the aerojet source.

This new method has high potential for the determination of structures using a stream of microcrystals synchronized with a pulsed X-ray laser or, in the long term, a stream of oriented and hydrated single protein molecules could be used, which

would allow for the study of the diffraction patterns in the transition to the 'gas phase'. In this regime, particle-size line broadening prevents identification of the reciprocal lattice and molecular alignment is required. Pending final development of alignment methods for serial crystallography, we show here that X-ray diffraction data may be obtained using our aerojet of small protein crystals without alignment, by applying the methods of powder diffraction to submicrometer crystallites within the droplets. Since the dimensions and symmetry of the unit cell can be determined from the ring pattern, powder diffraction avoids the need to solve the molecular alignment problem. Ultimately this is traceable to the fact that there is a finite number of Bravais lattices because there is a limited number of ways to arrange points periodically in space with identical environments. There is no such constraint for a single molecule.

These diffraction experiments were carried out using 530 eV X-rays with both 50 nm gold nanospheres and crystals of the membrane protein photosystem I with sizes of less than 500 nm. The use of such long wavelengths, particularly in the water window, increases the scattering cross section (thereby decreasing exposure times and particle concentrations needed) and reduces the effects of solution scattering. Gold spheres were used as a test object to optimize nozzle performance and data acquisition and analysis techniques. A theoretical simulation of the experiment fits the gold diffraction pattern and provides structural information that closely agrees with the manufacturer's analysis. The protein crystals were size restricted with a nanoporous filter to sizes of around 500 nm. Our preliminary experimental geometry and the long wavelength of the soft X-rays only allows for observation of the lowest-order diffraction rings but our results closely match theoretical predictions from the known structure.

2. Experimental

Diffraction data were collected at beamline 9.0.1 of the Advanced Light Source where the beam-defining optics are optimized for coherent soft X-ray scattering experiments (Fig. 1). The source, a 10 cm-period undulator with 43 periods, provides 530 eV photons in the third harmonic with an approximate photon flux of 10^{12} photons s^{-1} in a $50 \mu\text{m}$ focus provided by a monochromatizing zone plate segment. The combination of a nickel-coated relay mirror and beryllium vacuum window acts as a bandpass filter that removes higher and lower undulator harmonics while the remaining undulator spectrum is dispersed vertically by the off-axis zone plate segment. This $550 \mu\text{m}$ -diameter zone plate segment focuses the third undulator harmonic to a $50 \mu\text{m}$ spot one inch upstream of the droplet beam. This spot is then selected with a $50 \mu\text{m}$ pinhole. Experiments requiring greater transverse and longitudinal coherence use smaller beam-defining pinholes so that fewer coherent modes may be selected. Accepting the full undulator harmonic results in a bandwidth equal to the source bandwidth that is approximately equal to $1/mN$ where m is the harmonic number and N is the number of undulator periods. This neglects electron beam size and divergence and for our

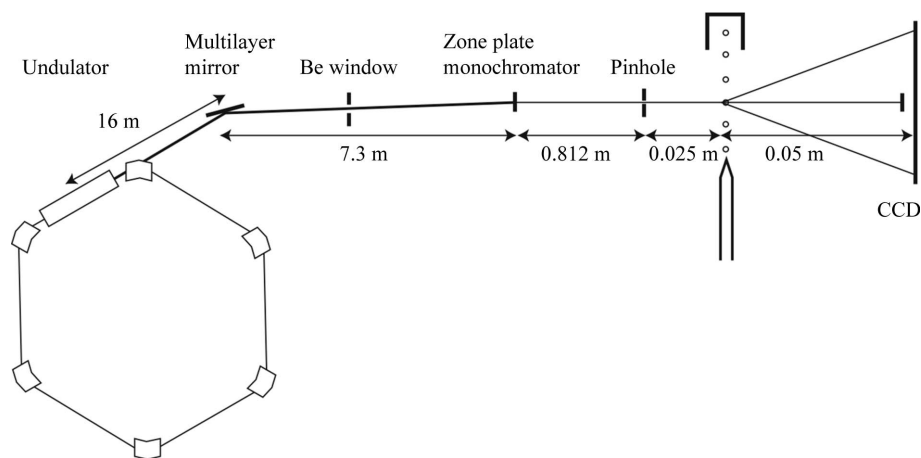


Figure 1

Beamline layout. The monochromator focuses the undulator beam in the vicinity of the droplet source for maximum photon flux and the 1 square inch detector is located 5–10 cm downstream. A multilayer mirror provides a Bragg reflection at 1500 eV and specular reflection in the energy range 500–800 eV.

case provides an upper limit on the bandwidth of 0.8%, though the actual value will not be significantly different.

Focusing of the X-ray beam is essential because of the flux-limited nature of this experiment. The beam divergence, dominated by the zone plate focusing with focal length of 80 cm and the large X-ray bandwidth, results in significant angular broadening of the scattered peaks. An undulator source at the ALS has a central cone divergence of approximately 40 μrad , which is at least a factor of 20 smaller than the other sources of beam spread. At the largest scattering angles recorded (12°), the angular width of a scattered beam is at least 0.13°, though the precise value is not known without a quantitative measurement of the X-ray monochromaticity. The detector used, a Princeton Instruments MTE2-1300B CCD, has sufficient angular resolution to make accurate measures of the powder peak profiles. The 20 μm pixels, at a 9 cm working distance, provide an angular resolution of 0.01° or 11.5 detector pixels per peak FWHM. Therefore, the detector was binned by a factor of four in each dimension for faster readout.

The particles of interest are delivered to the X-ray beam in a continuous liquid jet which breaks into droplets further downstream owing to a Rayleigh necking instability (Rayleigh, 1878). The jet, which is described in detail elsewhere (Weierstall *et al.*, 2008), consists of a column of particle-containing solution which flows through a 50 μm -inner-diameter hollow tube (fiber optic) and is accelerated upon exiting the tube by a coaxial flow of carbon dioxide gas into vacuum. The CO_2 , which acts to focus the liquid stream, condenses as dry ice on a liquid-nitrogen-cooled coldtrap, thereby minimizing the rise in pressure caused by the liquid and gas leak into the vacuum chamber. The acceleration by co-flowing gas thus serves the purpose of reducing the jet diameter while allowing use of a larger nozzle, which is less likely to clog. A typical jet diameter for the images shown here was 10 μm , which corresponds to a flow rate of a few tens of microliters per minute. Fig. 2(a) shows a liquid jet emerging

from the nozzle exit, averaged over an exposure time of 1 s, while Figs. 2(b) and 2(c) show flash (nanosecond) images of the droplets some greater distance from the nozzle tip. In Fig. 2(b) we have controlled the droplet generation rate using a piezoelectric actuator, which may be synchronized to a pulsed X-ray source for experiments aimed at reading out the diffraction pattern from single molecules, using a very fast read-out area detector (Neutze *et al.*, 2000; Shneerson *et al.*, 2008). However, for the results reported here, the droplet breakup was untriggered and occurred with the intrinsic Rayleigh instability frequency.

3. Data and analysis

Completed one-dimensional datasets are reduced from dozens of individual two-dimensional CCD recordings. The dynamic range of the CCD is significantly lower than that of the diffraction patterns so data must be collected on multiple time scales and then stitched together during post-processing. Furthermore, taking multiple CCD recordings for each exposure time and then averaging the results improves statistics. The centers of the diffraction patterns are found experimentally by attenuating the incident beam and then taking a direct measurement of its position on the CCD. This position can then be fine-tuned to subpixel resolution by calculating the center of mass of the scattering pattern. During normal data acquisition the direct beam is not attenuated and must be blocked by a beamstop to avoid damaging the sensitive detector, and therefore the data at very small scattering angles is lost. The center position is then used for a radial averaging procedure that produces the final dataset from the assembled two-dimensional diffraction patterns.

Scattering from the solution in which the particles are embedded leads to a background signal. The strongest contribution to the diffraction pattern from the solution results from total external reflection at the solution's surface. The proximity of the nozzle tip to the X-ray beam can be adjusted so that various points along the jet path can be probed. Diffraction patterns from the continuous jet immediately adjacent to the tip (a continuous column of liquid) show a sharp vertical streak owing to X-rays scattered from the horizontal jet's surface. X-rays scattered from the solution's interior are detected in all scattering directions and are significantly weaker. If, instead, the droplet region of the jet is probed, then the surface scattering is also isotropic, producing a disc of scattering reflected from a thin band around each droplet at the specular external reflection condition. The cut-off radius of this diffraction disc is set by the critical angle for external reflection. At higher beam energies, this cut-off and the disc diameter shrink rapidly. At our low energy, the disc greatly decreases the signal-to-noise ratio since it is only

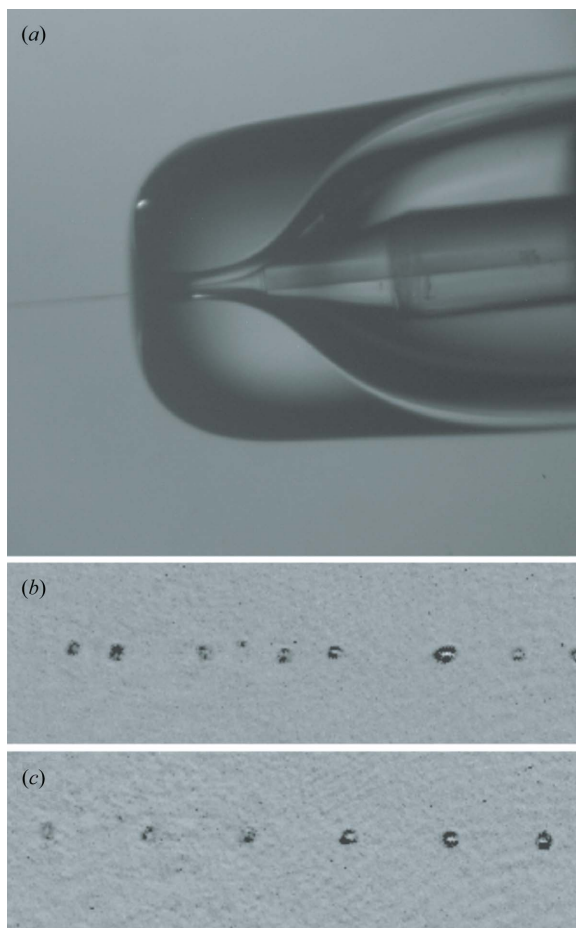


Figure 2
 (a) Aerojet droplet source. An inner capillary, a hollow fiber-optic with 50 μm inner diameter, carries the particle solution which is pressurized to 150 PSI. The outer glass capillary carries the focusing CO₂ gas at 15 PSI, which expands into vacuum producing a small jet of solution that breaks up into droplets. (b) Flash image (100 ns exposure time) of the untriggered droplets which are unevenly spaced and have a distribution of sizes. (c) Triggered droplets are evenly spaced and have a much narrower size distribution.

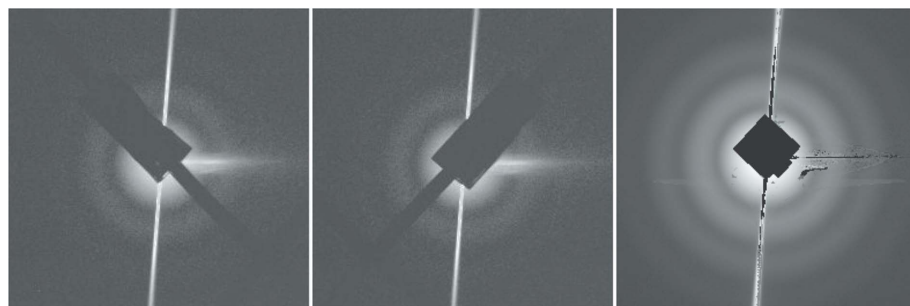


Figure 3
 Assembly of two-dimensional diffraction patterns. Full datasets are collected by the use of two beamstops that are oriented at 90° to each other. The vertical streaks are X-ray scatter from the continuous column of liquid leaving the nozzle gas aperture. Photons detected outside of those streaks originate from the particles within the buffer solution. Photons scattered off the nozzle tip form a bright horizontal streak to the right of the beamstop. Many patterns are averaged and data from opposing beamstops are merged to give the final dataset on the right. This process is not necessary for particles with isotropic scattering patterns but becomes essential if the particles scatter non-isotropic and are aligned.

particle scatter that we are interested in. For this reason, all experiments were carried out using the continuous jet.

3.1. Gold nanospheres

Initial experiments were performed using gold nanospheres as test objects to verify the integrity of the structural information obtained by this technique. The spheres (Ted Pella, part No. EM.GC50) were 50 nm in diameter and had a concentration of 4.5×10^{10} particles mL⁻¹. A flow rate of 30 μL min⁻¹ implies 2.3×10^7 balls s⁻¹ passed through the X-ray beam. Assuming a liquid flow speed of 10 m s⁻¹ and a 50 μm-wide X-ray beam, this indicates that 120 gold balls were continuously present in the beam at any instant. The motion of the balls does not affect the far-field diffraction pattern because the binned CCD pixels are larger than the X-ray beam diameter; therefore the exposure time is identical to that of 120 stationary balls in the X-ray beam. (Similar considerations also apply to proteins, which, because they are continually refreshed, avoid damage.) This number indicates that the aerojet is a sample with sufficient strength to be readily measured with our available flux. Indeed, the maximum exposure time used in this experiment was 1.5 s and provided scattered intensity to the edge of our detector. The total exposure after averaging was about 30 s. It is worth noting that the exposure time of any single gold ball in the sample was only 5 μs.

Fig. 3 describes the data reduction process. The system was designed with the intention of collecting diffraction patterns from streams of aligned particles (Spence & Doak, 2004). In the case of aligned particles it is necessary to record intensities on the two-dimensional detector at all points around the incident beam. Thus, the beamstop was designed to provide this functionality through the acquisition of two separate patterns at different beamstop positions. The shadow of the beamstop is rotated by 90° between the two positions and when merged leaves only a square of missing data at the very center of the diffraction pattern. Diffraction data are collected with the droplet beam on and with the droplet beam off for background subtraction. The pixels in the areas of very high noise, near nozzle tip scatter and jet scatter, are not reliable and so are masked before calculating the radial average.

The use of very long wavelengths and large scattering angles means that Ewald sphere curvature effects will be present in the recorded diffraction patterns. The spatial frequencies recorded lie on a sphere in reciprocal space that is described by

$$q_z = (1/\lambda)[(1/\lambda^2) - q_y^2 - q_x^2]^{1/2}.$$

Since the scattered intensities are recorded on a plane, they represent a gnomonic projection of the Ewald

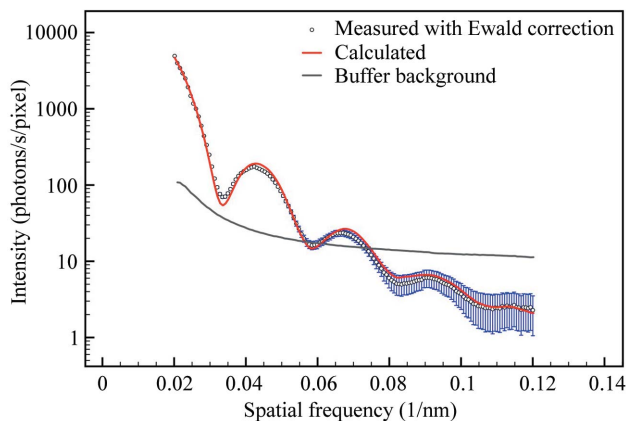


Figure 4

Radial average of Fig. 3. The circles are experimental data after background subtraction and the continuous red curve is calculated from a simulated diffraction pattern. The simulation represents an ensemble of gold spheres with normally distributed diameters with central diameter of 50.3 nm and standard deviation of 3.8 nm. This is in close agreement with the manufacturer's analysis, which claims 8% coefficient of variation. The solid grey curve shows the scattering pattern from a gold buffer solution for gold spheres that was subtracted as background from the gold particle pattern.

sphere and are offset radially by a distance in q -space that increases with scattering angle. This offset is given approximately by $\lambda^2 q^3/2$ where $q = (q_x^2 + q_y^2)^{1/2}$ is in the detector plane. At the maximum spatial frequencies recorded we then have $\Delta q/q = 0.04$. Fig. 4 shows the result of radially averaging the final pattern in Fig. 3 where the spatial frequencies indicated on the horizontal axis have been corrected for Ewald sphere curvature. The solid curve is a simulated diffraction pattern calculated from an ensemble of gold spheres with normally distributed diameters centered on 50.3 nm and a standard deviation of about 3.8 nm. The manufacturer of the particles (Ted Pella Inc., <http://www.tedpella.com/>) claims a coefficient of variation of less than 8%, which is in close agreement with our analysis.

3.2. Photosystem I protein nanocrystals

Photosystem I crystal samples were prepared from the cyanobacterium *Thermosynechococcus elongatus* as described elsewhere (Jordan *et al.*, 2001). Briefly, the cells were grown under low-light conditions to allow for a high yield of trimeric photosystem I. The cells were harvested, lysed, and the proteins extracted with detergent (β -dodecylmaltoside) and isolated using an anion-exchange chromatograph. The eluent solutions were composed of 20 mM MES pH 6.4, 0.02% (m/v) β -dodecyl maltoside, and a $MgSO_4$ gradient was used for the eluation of the protein. After purification, the photosystem I was diluted to low-salt conditions [final concentration of 20 mM MES pH 6.4, 6 mM $MgSO_4$ and 0.02% (m/v) β -dodecyl maltoside], which leads to the growth of micrometer- and submicrometer-sized crystals spontaneously overnight at 277 K.

The size of the photosystem I crystallites was then restricted by placing a 500 nm filter in the liquid line of the aerojet. With

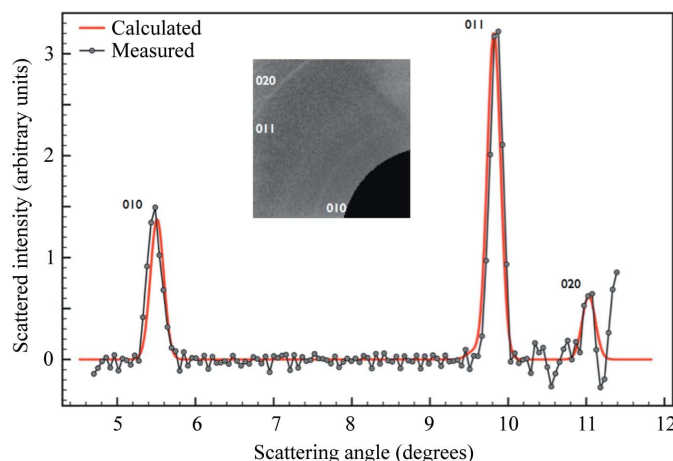


Figure 5

Powder pattern from photosystem I nanocrystals with sizes of about 500 nm. The measured q -vectors have Miller indices of 010, 011 and 020. The solid red curve represents a calculated powder pattern and is in good agreement with experiment when scaled so that they have equal maximum intensities. The inset shows a subset of the experimental data with background subtracted.

many such crystallites per droplet, the recorded diffraction pattern contains contributions from crystallites in all possible orientations. This generates a sphere centered on the origin of reciprocal space for every reciprocal lattice point, which is intersected on a circle by the Ewald sphere, producing the familiar Debye–Scherrer diffraction rings. In reality, this sphere is a shell of finite thickness, which depends on several experimental factors. These include beam divergence, spectral bandwidth, crystallinity effects such as imperfections or finite crystal size, and instrumental broadening resulting from finite angular resolution. Fig. 5 shows powder diffraction peaks corresponding to (010), (011) and (020) reflections. The (011) peak at 9.9° overlaps with the (110) peak at 9.6°. The latter is manifested by a small asymmetric left shoulder and constitutes 2% of the peak area. As noted earlier, the peak width due to the characteristics of the X-ray illumination is 0.13°. In Fig. 5 the measured powder peaks have FWHM widths of about 0.25°. The additional peak width must therefore result from crystallinity and finite size effects. If the small crystallites are coherently illuminated then the Bragg peaks will be convolved with the diffuse coherent scatter that represents the overall crystal morphology. Averaging this effect over many such crystals will give a broadened powder profile whose width is inversely proportional to the average crystal size. The number of coherent modes in our beam is given approximately by

$$N = 2xx'/\lambda,$$

where x is the beam size in the monochromator focus and x' is the beam divergence. This gives 27 coherent modes in our 50 μm beam or about 2 μm per mode. Thus, all the crystallites are coherently illuminated and it is not likely that neighboring crystals interfere coherently. The average crystal size associated with our observed angular spread is $d = \lambda/\theta = 585$ nm and corresponds to photosystem I crystals with $19 \times 19 \times 32$ unit cells, or about 23000 molecules per crystal. The exposure

time for the diffraction pattern was only 30 s, with a flow rate of $10 \mu\text{L s}^{-1}$, *i.e.* only very small amounts of samples (0.3 ml) have been used for the diffraction pattern. This small sample volume would allow the development of the use of the droplet stream for the high-throughput robotic screening of crystallization drops for microcrystals that are not visible by optical microscopy.

The projection of three-dimensional data onto one dimension in powder diffraction results in a loss of information in two ways (see David *et al.*, 2002, for a review). First, at large angles the decreasing ring spacing eventually becomes less than the angular resolution of the instrument, setting a limit on the ultimate resolution of the density map. Second, overlaps can occur in space groups of higher symmetry than orthorhombic owing to indexing accidents, so that structure factors of different magnitude contribute to the same ring. Degeneracies owing to point, space-group and chiral symmetries may also be masked, and these must be known to extract structure factor magnitudes unless, as in the charge-flipping method, the analysis is always performed in *P1*. In a previous paper (Wu *et al.*, 2006), we have shown how a variant of this charge-flipping algorithm can resolve both the accidental degeneracies and the symmetry degeneracy in powder data from inorganic crystals. The most common space group for proteins is orthorhombic $P2_12_12_1$, which has no accidental overlaps. The density of reciprocal lattice points for a triclinic crystal may be found as a function of scattering angle $\theta = 2 \sin^{-1}(\lambda/2d)$ (twice the Bragg angle Θ_B) as (David *et al.*, 2002)

$$\frac{\Delta N}{\Delta \theta} = \frac{16\pi V \sin^2(\theta/2) \cos(\theta/2)}{\lambda^3}.$$

Thus peak density is proportional to the square of the scattering angle for small angles, inversely proportional to d^2 (for $d < \lambda$), proportional to cell volume, and inversely proportional to λ^3 . This function has a maximum at $\Theta_B = 55^\circ$, where $\Delta N \simeq 19 \text{ V}$ per degree for hard X-rays around $d = 1 \text{ \AA}$. Our use of long wavelength (2.3 nm) thus greatly improves peak separation, while limiting ultimate resolution (an upgrade to 4 Å wavelength is planned). This improves angular resolution owing to beam divergence, but not owing to particle-size broadening, which is independent of beam energy. We use an undulator insertion device for high flux (focused to the 20 μm -diameter of our droplet beam), and take advantage of the λ^4 dependence of coherent scattered intensity (Howells *et al.*, 2008). This enables short exposure times from our droplets, which contain relatively few protein molecules. The solution of such large proteins by powder methods at low resolution may best be attacked by using a combination of parameterized theoretical modeling, molecular replacement and/or isomorphous replacement.

4. Conclusion

We have demonstrated for the first time solution X-ray scattering from a microjet of nanoscale crystallites of a membrane protein using a synchrotron undulator source. For non-crystallized particles, this procedure yields the equivalent of a

small-angle X-ray scattering pattern while for small crystallites it yields a powder diffraction profile. Our analysis shows that quantitative structural information may be obtained from the scattering data acquired in this manner. The primary benefit of this technique is that the smallest available protein crystals may be used without any concern for radiation damage in a windowless geometry which provides an optical path short enough for use of medium-energy X-rays. Temperature variation along the jet may also be used to aid in peak deconvolution. Currently, there is no other X-ray scattering technique that can utilize such small crystals with such ease. Furthermore, shorter wavelengths and the possible use of particle alignment schemes (Kisilak *et al.*, 2001), currently under development, may allow for the *ab initio* phasing of these diffraction patterns (Shapiro *et al.*, 2005) and provide structural maps in the several angstrom range. The incident flux density required for X-ray imaging is inversely proportion to λ^2 while the dose (energy deposited per unit mass) is relatively independent of energy from 1–10 keV. This seems to indicate that the lowest energies compatible with the desired resolution should be used. Recent theoretical simulations show that 7 Å resolution should be obtainable using planned undulator sources with energies of around 3 keV (Starodub *et al.*, 2008).

The aerojet droplet source, being a very high brightness particle beam, is also ideally suited for experiments with pulsed X-ray sources. The triggered droplet beam may be precisely synchronized to the X-ray pulses so that all proteins are utilized. This is in contrast to electrospray injection schemes that produce a highly divergent particle beam and cannot be synchronized. Furthermore, the remaining water layer surrounding the proteins may be continuously adjusted by altering the transit time, *i.e.* evaporation time, between droplet source and X-ray beam. It has been suggested that this water layer may act as a tamper to slow the explosion of proteins in such intense X-ray pulses and allow the use of longer pulses for the acquisition of atomic-resolution diffraction data (Hau-Riege *et al.*, 2007). Finally, this aerojet device produces a stream of uncharged particles and thereby eliminates possible damage to the molecules associated with the high molecular charge as observed in electrospray mass spectroscopy.

We graciously acknowledge support from the staff of the Advanced Light Source at Lawrence Berkeley National Laboratory. This research is supported by grants from The Center for Biophotonics Science and Technology at the University of California at Davis, the National Science Foundation (IDBR-0555845) and ARO (W911NF-05-1-0152). The Advanced Light Source at Lawrence Berkeley National Laboratory is supported by the Director, Office of Science, Office of Basic Energy Sciences, Materials Sciences Division, of the US Department of Energy. The structural project on photosystem I is supported by the National Science Foundation, grant number 0417142.

References

- David, W., Shankland, K., McCusker, L. & Baerlocher, Ch. (2002). *Structure Determination from Powder Diffraction Data*. Oxford University Press.
- DePonte, D. P., Weierstall, U., Starodub, D., Warner, J., Spence, J. C. H. & Doak, R. B. (2008). *J. Appl. Phys.* In the press.
- Hau-Riege, S. P., London, R. A., Chapman, H. N., Szoke, A. & Timneanu, N. (2007). *Phys. Rev. Lett.* **98**, 198302.
- Henke, H., Gullikson, E. & Davis, J. (1993). *Atom. Data Nucl. Data Tables*, **54**, 181–342.
- Howells, M. R., Beetz, T., Chapman, H. N., Cui, C., Holton, J. M., Jacobsen, C. J., Kirz, J., Lima, E., Marchesini, S., Miao, H., Sayre, D., Shapiro, D. A. & Spence, J. C. H. (2008). *J. Spectrosc. Relat. Phenom.* In the press.
- Jordan, P., Fromme, P., Witt, H. T., Klukas, O., Saenger, W. & Krauss, N. (2001). *Nature (London)*, **411**, 909–917.
- Kisilak, M., Anderson, H., Babcock, N., Stetzer, M. & Idziak, S. (2001). *Rev. Sci. Instrum.* **72**, 4305–4307.
- Margiolaki, I. & Wright, J. P. (2008). *Acta Cryst.* **A64**, 169–180.
- Margiolaki, I., Wright, J. P., Wilmanns, M., Fitch, A. N. & Pinotsis, N. (2007). *J. Am. Chem. Soc.* **129**, 11865–11871.
- Neutze, R., Wouts, R., van der Spoel, D., Weckert, E. & Hadju, J. (2000). *Nature (London)*, **406**, 752–757.
- Rasmussen, S. G., Choi, H. J., Rosenbaum, D. M., Kobilka, T. S., Thian, F. S., Edwards, P. C., Burghammer, M., Ratnala, V. R., Sanishvili, R., Fischetti, R. F., Schertler, G. F., Weis, W. I. & Kobilka, B. K. (2007). *Nature (London)*, **445**, 383–387.
- Rayleigh, L. (1878). *Proc. London Math. Soc.* **10**, 4–13.
- Shapiro, D., Thibault, P., Beetz, T., Elser, V., Howells, M., Jacobsen, C., Kirz, J., Lima, E., Miao, H., Neiman, A. & Sayre, D. (2005). *Proc. Nat. Acad. Sci.* **102**, 15343.
- Shneerson, V. L., Ourmazd, A. & Saldin, D. K. (2008). *Acta Cryst.* **A64**, 303–315.
- Spence, J. C. H. & Doak, R. B. (2004). *Phys. Rev. Lett.* **92**, 198102.
- Starodub, D., Rez, P., Hembree, G., Howells, M., Shapiro, D., Chapman, H. N., Fromme, P., Schmidt, K., Weierstall, U., Doak, R. B. & Spence, J. C. H. (2008). *J. Synchrotron Rad.* **15**, 62–73.
- Von Dreele, R. B. (2007). *J. Appl. Cryst.* **40**, 133–143.
- Von Driel, R. (2007). Personal communication.
- Weierstall, U., Doak, R. B., Spence, J. C. H., Starodub, D., Shapiro, D., Kennedy, P., Warner, J., Hembree, G. G., Fromme, P. & Chapman, H. N. (2008). *Exp. Fluids*. In the press.
- Wu, J., Leinenweber, K., Spence, J. C. H. & O’Keeffe, M. (2006). *Nat. Mater.* **5**, 647–652.